

# THE INFLUENCE ON FINITE MEASUREMENT ACCURACY ON THE SWE-TO-PWE ANTENNA DIAGNOSTICS TECHNIQUE

C. Cappellin<sup>(1-2)</sup>, O. Breinbjerg<sup>(1)</sup>, A. Frandsen<sup>(2)</sup>

<sup>(1)</sup> Ørsted•DTU, Technical University of Denmark, DK-2800 Kgs. Lyngby, Denmark  
<sup>(2)</sup>TICRA, Læderstræde 34, DK-1201, Copenhagen, Denmark

## ABSTRACT

A new antenna diagnostics technique based on the transformation of the spherical wave expansion (SWE) into the plane wave expansion (PWE) is proposed. The new technique allows the recovery of the plane wave spectrum in the visible region, and in principle also in part of the invisible region, from data acquired during a spherical near-field measurement. From the PWE the aperture field can subsequently be calculated. While the fundamental properties of the SWE-to-PWE transformation have been reported in previous articles, we concentrate here on the influence of non-ideal measurements aspects on this diagnostics technique. In order to isolate different measurement inaccuracies, the investigation is based on simulations.

## 1. INTRODUCTION

While the effect of electrical or mechanical errors in an antenna is observed in its measured far-field pattern, the errors themselves are more easily identified in the extreme near-field of the antenna. Several non-invasive diagnostics techniques have been proposed over the years [1]-[3], but generally these techniques possess limitations with respect to the type of antennas and antenna errors to which they apply, and/or to the accuracy they provide.

We have proposed a new diagnostics technique [4]-[5] to be applied at the DTU-ESA Spherical Near-Field Antenna Test Facility located at the Technical University of Denmark [6]. The measurement technique employed at the DTU-ESA Facility is based on the SWE of the field radiated by the antenna. The SWE is valid outside the antenna minimum sphere and does not readily allow the calculation of the aperture field in the extreme near-field of the antenna. One way to overcome this is to transform the SWE of the radiated field into a PWE. The plane wave spectrum can be computed from the knowledge of the coefficients of the SWE, on any aperture plane in the extreme near-field outside the antenna. This technique gives two main advantages. The first is that the plane wave spectrum can in principle be evaluated also in part of the spectrally invisible region, and the second is that the aperture field can be computed as an Inverse Fourier Transform (IFT) of this

spectrum. Hence, the spatial resolution achieved in the aperture field can theoretically exceed the traditional limit of half a wavelength. While the fundamental properties of the SWE-to-PWE transformation have been described in previous articles [4]-[5], we will concentrate here on how non-ideal measurements aspects affect the diagnostics technique. To do that, we will consider an antenna model consisting of electric and magnetic Hertzian dipoles. Noise and electrical measurements inaccuracies will be added to the calculated near-field. The effects of such quantities on the obtained  $Q$  coefficients and on the extreme near-field provided by the diagnostics will be then studied. Finally, errors will be introduced in the antenna model and the ability of the diagnostics technique to identify these will be tested. All results are expressed in the S.I. rationalized system with the  $e^{-i\omega t}$  time convention.

## 2. THEORY OF THE SWE-TO-PWE TRANSFORMATION

We begin by introducing the SWE of the electric field  $\bar{E}$  radiated by an antenna circumscribed by a minimum sphere of radius  $r_o$  [7],

$$\bar{E}(\bar{r}) = \frac{k}{\sqrt{\eta}} \sum_{n=1}^{\infty} \sum_{m=-n}^n Q_{1nm}^{(3)} \bar{F}_{1nm}^{(3)}(\bar{r}) + Q_{2nm}^{(3)} \bar{F}_{2nm}^{(3)}(\bar{r}), \quad r > r_o \quad (1)$$

where  $Q_{1nm}^{(3)}$  and  $Q_{2nm}^{(3)}$  are the expansion coefficients, obtained from a spherical near-field measurement, and  $\bar{F}_{1nm}^{(3)}(\bar{r})$  and  $\bar{F}_{2nm}^{(3)}(\bar{r})$  are the power-normalized spherical vector wave functions. The medium intrinsic admittance is  $\eta$ ,  $k$  is the wave number, and  $\bar{r}$  is the position vector expressed in terms of spherical coordinates  $(r, \theta, \varphi)$  or rectangular coordinates  $(x, y, z)$ . In practice, the  $n$ -summation of the SWE is truncated at  $N=kr_o+10$  since this is sufficient for an accurate calculation of the far-field. The PWE of the same electric field  $\bar{E}$  in the spectral  $k_x, k_y$ -domain valid for  $z > z_o$ , with  $z_o$  being the largest  $z$ -coordinate of the antenna, is given by [8]

$$\bar{E}(x, y, z) = \frac{1}{2\pi} \int_{-\infty}^{\infty} \int_{-\infty}^{\infty} \bar{T}(k_x, k_y) e^{ik_z z} e^{i(k_x x + k_y y)} dk_x dk_y \quad (2)$$

where  $k_x$  and  $k_y$  are the spectral variables and  $k_z = \sqrt{k^2 - k_x^2 - k_y^2}$ . The spectral domain can be divided in two regions, the visible, for  $k_x^2 + k_y^2 \leq k^2$ , containing the propagating plane waves, and the invisible, for  $k_x^2 + k_y^2 > k^2$ , containing the evanescent plane waves, see Fig. 1. The two variables  $k_x$  and  $k_y$  are always real, while  $k_z$  is real in the visible region but purely imaginary with a positive imaginary part in the invisible region. In practice, the  $k_x$ - and  $k_y$ -integrals are truncated at finite values  $\pm k_{xmax}$  and  $\pm k_{ymax}$  respectively. At the border between the visible and invisible regions  $k_z = 0$  and the PWE generally possesses a singularity there [8].

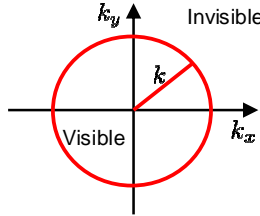


Figure 1. Visible and invisible regions of the spectral  $k_x, k_y$ -domain.

The plane wave spectrum for a given  $z$ -coordinate is thus  $\bar{T}(k_x, k_y)e^{ik_z z}$ . It was previously shown [4][9] how the SWE of Eq. 1 can be transformed into the PWE of Eq. 2, arriving at the following relation

$$\bar{T}(k_x, k_y)e^{ik_z z} = \frac{1}{k_z} \hat{E}(\hat{s}) \exp(ik \cos \alpha z) \quad (3)$$

where  $\hat{E}(\hat{s})$  is given by

$$\hat{E}(\hat{s}) = \sum_{n=-\infty}^{\infty} \sum_{m=-n}^n \frac{(-i)^n}{\sqrt{\eta} \sqrt{n(n+1)}} \left[ Q_{2nm}^{(3)} \hat{s} \times \bar{Y}_n^m(\alpha, \beta) + -i Q_{1nm}^{(3)} \bar{Y}_n^m(\alpha, \beta) \right] \quad (4)$$

with  $\hat{s} = \sin \alpha \cos \beta \hat{x} + \sin \alpha \sin \beta \hat{y} + \cos \alpha \hat{z}$ ,  $\beta \in [-\pi, \pi]$  and equal to  $\beta = \text{atan}(k_y / k_x)$ ,  $\alpha \in C_+$  see Fig. 2 and equal to  $\alpha = \text{acos}(k_z / k)$ , and  $\bar{Y}_n^m(\alpha, \beta)$  being the vector spherical harmonics, see also [4]-[5].

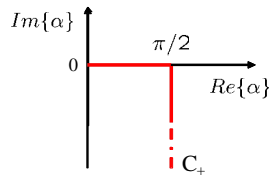


Figure 2. Domain of the variable  $\alpha$  on contour  $C_+$ .

The imaginary values of the angle  $\alpha$  correspond to the invisible  $k_x, k_y$ -domain, and make the spherical harmonics  $\bar{Y}_n^m(\alpha, \beta)$  divergent in that region. Eq. 4 shows

that the plane wave spectrum can be expressed as a series of spherical harmonics weighted by the  $Q$  coefficients of the SWE of the radiated field. But, while the visible region of the spectrum converges around  $N=kr_o$ , the invisible requires many more modes [5]. In practice the high order modes can not be measured due to the finite dynamic range. However, it has been shown [5] that the recovery with  $N \approx kr_o$  terms of the visible region and the singularity for  $k_z = 0$  provides accurate aperture fields. The spatial resolution  $(\delta_x, \delta_y)$  obtained in the aperture field is given by  $\delta_x = \pi / k_{xmax}$ ,  $\delta_y = \pi / k_{ymax}$  and can in principle be controlled by selecting  $k_{xmax}$  and  $k_{ymax}$  appropriately in the SWE-to-PWE transformation. While in previous works [4]-[5] the investigations were based on ideal noise-free test cases, we will concentrate in the following on more realistic cases.

## 2.1. SIMULATION MODEL FOR FINITE MEASUREMENT ACCURACY

It is the purpose of this section to consider some of the most typical measurement electrical inaccuracies in order to clarify their influence on the proposed diagnostics technique. To do that, a Standard Gain Horn (SGH) model consisting of electric and magnetic Hertzian dipoles will be considered. Different measurement electrical errors will be added to its radiated near-field and from that field distribution the  $Q$  coefficients will be computed. The aperture field will be then calculated by using Eqs. 2-3-4.

## 2.2. Antenna Model

The SGH model works at the frequency of 3GHz. It represents a pyramidal horn with an aperture of  $a=4\lambda$  and  $b=3\lambda$  located on the  $xy$ - plane, see Fig. 3, and with the lengths of the flared section in the  $xz$ - and  $yz$ -planes being  $R_2=R_1=5\lambda$ . The dominant TE<sub>10</sub> mode constitutes the co-polar component, it is  $y$ -polarized and excited with amplitude 1, while the TE<sub>01</sub> mode provides a typical cross-polar component, it is  $x$ -polarized and has an amplitude of  $10^{-2}$  and a phase of  $-i\pi/4$ , see Fig. 3.

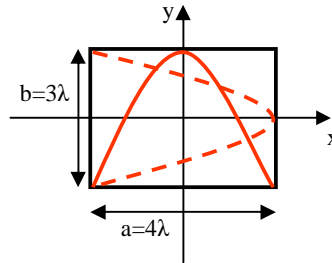


Figure 3. Aperture of the SGH model with the TE<sub>10</sub> and TE<sub>01</sub> modes, and the reference coordinate system.

From the equivalence theorem, the equivalent magnetic co-polar currents are

$$\bar{M}_{co} = \cos\left(\frac{\pi x}{a}\right) \exp\left(i\frac{k}{2}(x^2/R_2 + y^2/R_1)\right) \hat{x} \quad (8)$$

while the electrical are computed from the magnetic imposing a Huygens source dependence

$$\bar{J}_{co} = -\eta \cos\left(\frac{\pi x}{a}\right) \exp\left(i\frac{k}{2}(x^2/R_2 + y^2/R_1)\right) \hat{y} \quad (9)$$

with  $x \in [-a/2, a/2]$  and  $y \in [-b/2, b/2]$ . The cross-polar equivalent currents are computed in the same way and are equal to

$$\bar{J}_{cro} = -\eta \cos\left(\frac{\pi y}{b}\right) \exp\left(i\frac{k}{2}(x^2/R_2 + y^2/R_1)\right) \hat{x} \quad (10)$$

$$\bar{M}_{cro} = -\cos\left(\frac{\pi y}{b}\right) \exp\left(i\frac{k}{2}(x^2/R_2 + y^2/R_1)\right) \hat{y} \quad (11)$$

The current distributions of Eqs. 8-11, are sampled every  $\lambda/4$  on the  $xy$ -plane to provide on the sampling points the excitation of a set of electric and magnetic Hertzian dipoles distributed on the aperture. From this dipole distribution the radiated field is computed and the directivity is plotted, see Fig. 4. It can be seen that the model represents a typical SGH pattern both in the co-polar as well as in the cross-polar components, computed according to Ludwig 3<sup>rd</sup> definition [7].

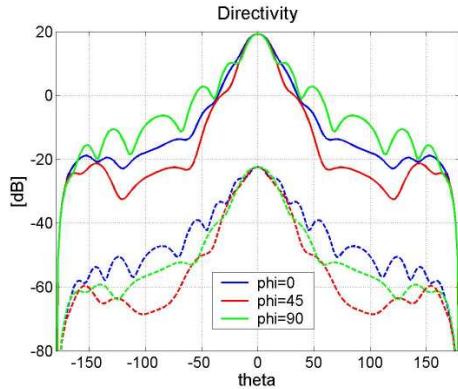


Figure 4. Directivity of the SGH model, co-polar (continuous lines), cross-polar (dashed lines).

### 2.3. Measurement Electrical Inaccuracies Model

Drift and noise, in amplitude and in phase, have been chosen to represent the most frequent and important measurement electrical inaccuracies. Their values are reported in Tab. 1, for a frequency of 3GHz and a scan speed of 3 deg/sec. The drift during a spherical scan has been modelled as a linear function of the time  $t$  given by  $drift_{error} = d \cdot t / T$ , with  $d$  being the value of the drift

(Tab.1), in amplitude or in phase, and  $T$  the duration of a scan.

Amplitude drift	-0.015 dB
Amplitude noise	-60 dB
Phase drift	0.25°
Phase noise	0.15°

Table 1. Measurement electrical inaccuracies values.

If  $X = |X|e^{i\angle X}$  is the  $\theta$ - or  $\phi$ -component of the electric field  $\bar{E}$  at a distance of  $10\lambda$  from the origin, then the field is equal to  $X_{tot} = (|X| \cdot (1 + drift_{error}))e^{i\angle X}$  when affected by amplitude drift and to  $X_{tot} = (|X|)e^{i(\angle X + drift_{error})}$  when affected by phase drift. The noise has been considered random and uniformly distributed providing  $X_{tot} = (|X| + noise_{error})e^{i\angle X}$  for the amplitude noise and  $X_{tot} = |X|e^{i(\angle X + noise_{error})}$  for the phase noise. The  $Q$  coefficients have then been computed from the near-field distribution with electrical inaccuracies by the software SNIPTD [10], and the power spectrum has been found, see Fig. 5. The

radiated power is equal to  $P_{rad} = \sum_{n=1}^N P_{rad}(n)$

with  $P_{rad}(n) = \frac{1}{2} \sum_{sm} |Q_{smn}^{(3)}|^2$ .

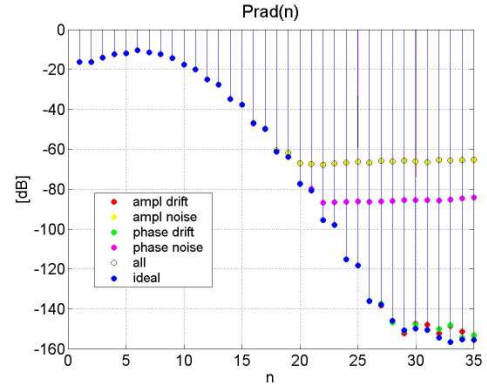


Figure 5. SGH power spectrum for different electrical inaccuracies and for the ideal inaccuracies-free case.

Fig. 5 shows that the major and most evident effect of the considered electrical inaccuracies is to truncate the available  $n$ -modes. It can be noted that numerical noise will anyway affect the computation, limiting the  $n$ -modes to  $N=28=kr_o+13$  for the ideal case. Since, all types of measurement errors manifest themselves as a constant level of the spectrum after a certain mode number, it was decided to continue the investigation with the amplitude noise alone, and then investigate different values of this.

## 2.4. Spectra and Near-Fields

The plane wave spectrum is then computed by using Eqs. 3-4 with the  $Q$  coefficients obtained from the field distribution affected by an amplitude noise of  $-60$  dB. The truncation in  $n$  is set equal to 18, and an aperture plane equal to  $z = 0.2\lambda$  is selected. A plot of the  $y$ - and  $z$ -components is reported in Fig. 6 in dB scale with the values normalized to  $T_y(0,0)$ , and compared to the ones calculated through the ideal case with a truncation in  $n$  equal to 28.

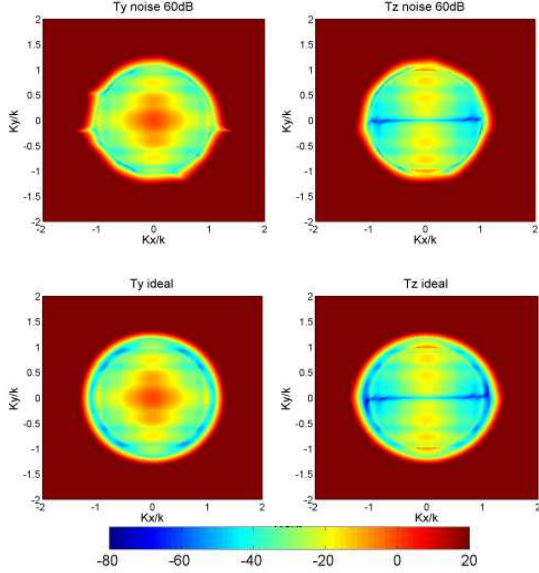


Figure 6. Amplitude of  $T_y$  and  $T_z$  on  $z=0.2\lambda$ , for a noise amplitude of  $-60$ dB (above) and for the ideal inaccuracies-free case (below).

In both cases the visible region is recovered, and the singularity at  $k_z = 0$  is identified. The extra ten  $n$ -modes, provided by an improvement of 80 dB in the dynamic range of the ideal case, allow the reconstruction of a small part of the invisible region, which reduces for the noisy case. The spectrum on the invisible domain is then replaced by zeros in the non-converging region and inverse Fourier transformed, see Fig. 7. For the data affected by amplitude noise the convergent region has a radius of  $1.03k$ , while for the ideal case it is  $1.1k$ . Fields are in dB scale and normalized to the value of  $E_y(0,0)$  when affected by amplitude noise. They are compared to the components given by the ideal case, and to the ones provided by the superposition of the analytical dipole contribution. The results affected by amplitude noise are satisfactory and in good agreement with the ideal and the analytical ones, both for the  $y$ - as well as for the  $z$ -component. Very accurate results are provided by the ideal case, where the convergent region has a radius of  $1.1k$ . We can again conclude that the recovery of the singularity for  $k_z = 0$  and of small part of the

invisible region are important to reconstruct the aperture field.

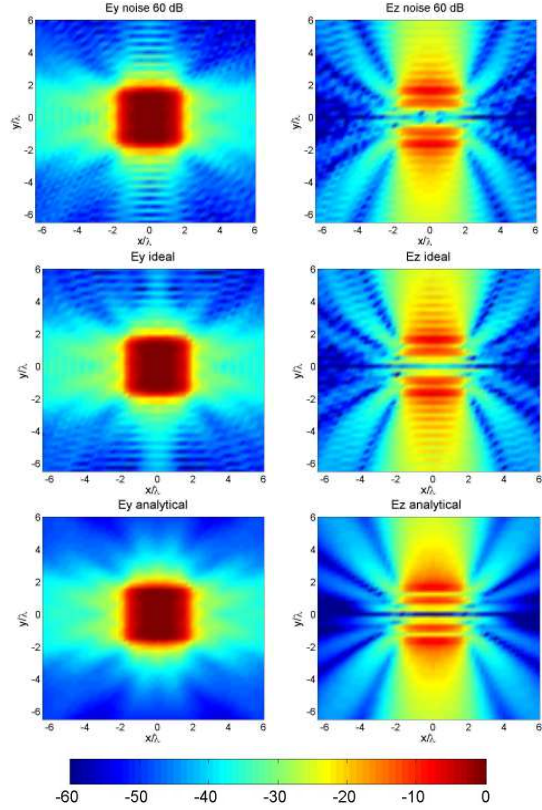


Figure 7. Amplitude of  $E_y$  and  $E_z$  on  $z=0.2\lambda$ , for a noise amplitude of  $-60$ dB (above), for the ideal inaccuracies-free case (center) and for the analytical case (below).

## 3. DIAGNOSTICS EXPERIMENT

The TE<sub>20</sub> mode is now introduced in the SGH aperture, to simulate an overmoding error, with an amplitude equal to 0.1 or 0.2. The presence of this error gives rise to an asymmetry both in the main lobe and the side-lobes of the directivity pattern, see Fig. 8. For every TE<sub>20</sub> amplitude case an amplitude noise varying between  $-70$  dB and  $-50$  dB is later added to the SGH near-field distribution at a distance of  $10\lambda$  from the origin. The  $Q$  coefficients are computed by SNIFTD [10] and the power spectrum is calculated, see Fig. 9. It can be seen that for a noise amplitude of  $-50$  dB we have  $N=17$  modes, and that a new mode is obtained every time the noise is decreased by  $-10$  dB. The effect is the same whether the amplitude of the TE<sub>20</sub> mode is 0.1 or 0.2. The spectral components are then computed on the plane  $z = 0.2\lambda$ , with the  $N$  truncation values of Tab. 2. For both amplitudes of the TE<sub>20</sub> mode and for all noise amplitudes, the visible region of the plane wave spectrum converges and the singularity is identified. For all cases, the effect in Eq. 4 of an extra mode in  $n$  reflects into an enlargement of the convergent

region of the invisible spectrum. For -50dB noise the reconstructed region has a radius of  $1,02k$  which becomes  $1,04k$  for -60dB and  $1.14k$  for the ideal case.

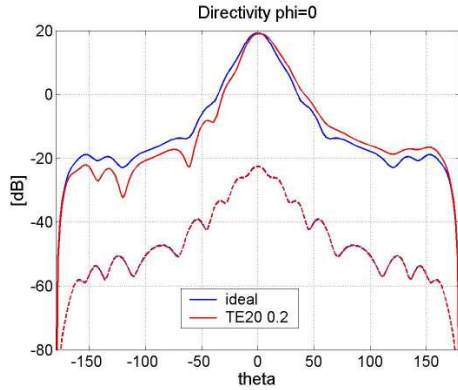


Figure 8. Directivity on  $\phi=0$  for the SGH with TE20 amplitude equal to 0.2: co-polar (continuous line), cross-polar (dashed line), in blue the ideal case with no overmoding.

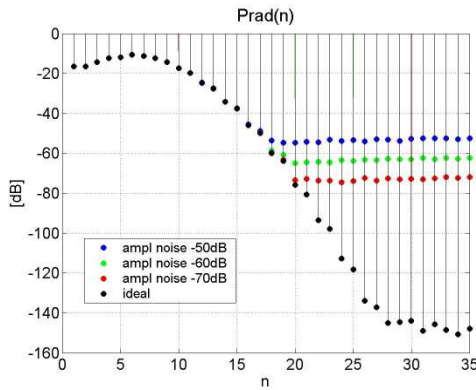


Figure 9. Power spectrum for different values of noise amplitude: SGH with TE20 amplitude equal to 0.2.

-50 dB amplitude noise	$N=17$
-60 dB amplitude noise	$N=18$
-70 dB amplitude noise	$N=19$

Table 2. Truncation value  $N$  for different amplitude noise.

The non convergent invisible domain is replaced by zeros and the spectral components are inverse Fourier transformed. Plots for the  $x$ - and  $y$ -components of the aperture field are shown in Fig.10 for the TE20 amplitude equal to 0.2, in dB scale and normalized to  $E_y(0,0)$  when -50 dB noise is present. The aperture distribution is compared to the one provided by the ideal case with no noise and  $N=27$ , and to the analytical dipole distribution. Different colour scales are used for the  $x$ - and  $y$ -components to better visualize the amplitude variations. The asymmetry in the aperture

distribution is clearly detected in both components, providing accurate results in comparison with the analytical ones. The importance of the detection of the singularity for  $k_z = 0$  is again noticed.

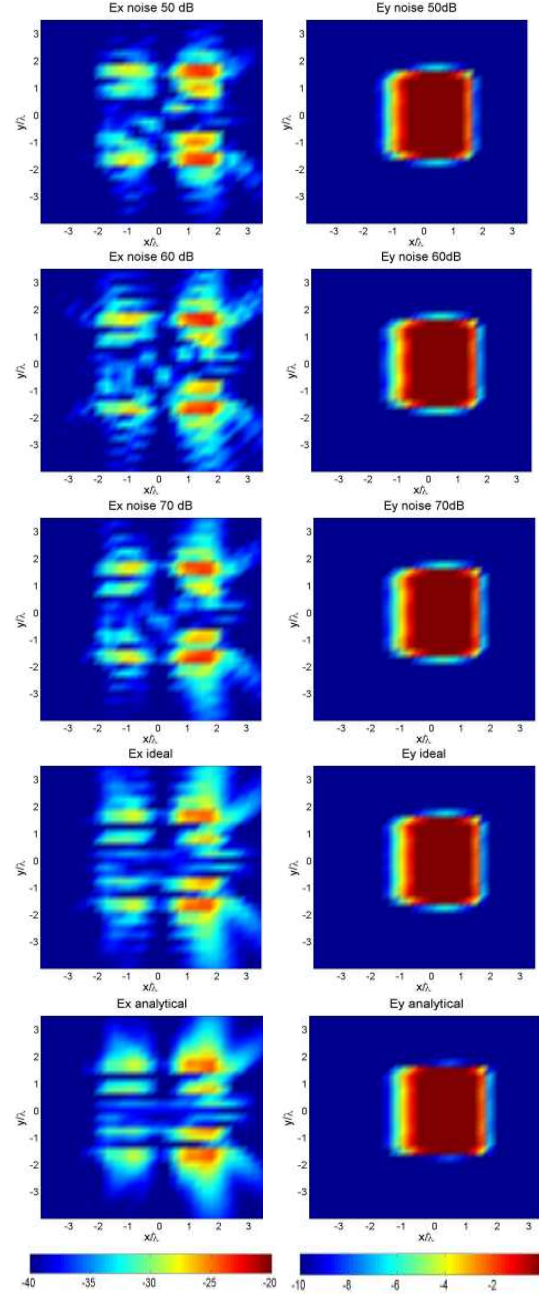


Figure 10. Amplitude of  $E_x$  and  $E_y$  on  $z=0.2\lambda$  for a TE20 amplitude of 0.2. From the top: noise amplitude -50dB, -60dB and -70dB, ideal inaccuracies-free case, and analytical case.

To underline its importance, for a diagnostics point of view, the radius of the converging region for -60dB noise is now selected first equal to  $0.8k$  and then  $0.95k$ ,

while all the remaining spectrum is replaced by zeros. The spectra are inverse Fourier transformed on  $z = 0.2\lambda$ , and the results are shown in Fig. 11, for the  $x$ -component. Even though an asymmetry is detected, the accuracy in respect to the ideal or the analytical case is very poor and not satisfactory. We can conclude that the singularity, well reconstructed by 17 modes, and a small part of the invisible domain are important for an accurate diagnostics technique.

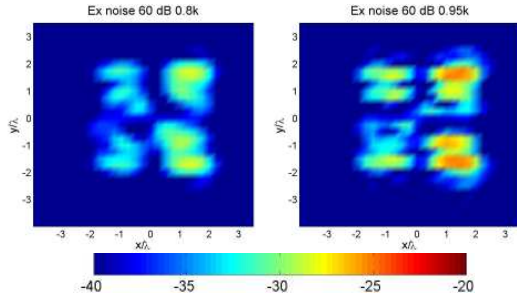


Figure 11. Amplitude of  $E_x$  on  $z=0.2\lambda$  for a TE20 amplitude of 0.2 and -60dB amplitude noise: convergent region of radius 0.8k (left), convergent region of radius 0.95k (right).

To support that the aperture field obtained in Fig. 10 is the consequence of an overmoding error and not of a mechanical tilt of the SGH aperture, the phase of the  $y$ -component is plotted, see Fig. 12. The symmetry of this on the  $xy$ -plane indicates that a tilt is not present.

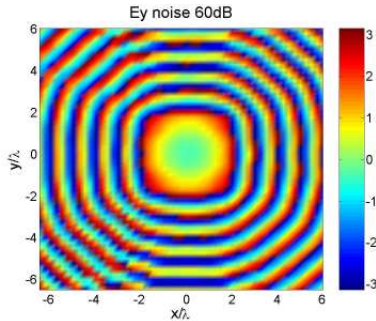


Figure 12. Phase of  $E_y$  on  $z=0.2\lambda$  for a TE20 amplitude of 0.2, -60dB amplitude noise and 1.04k convergent region.

#### 4. CONCLUSIONS

The effects of finite measurement accuracy on the SWE-to-PWE diagnostics technique have been presented. It was found that among the numerous kinds of measurement electrical errors, the amplitude noise was the strongest and the most important. The effect of such a noise distribution generally reflects into a truncation of the available  $Q$  coefficients of the SWE of the field. It has been found that for a SGH the measured  $Q$ 's are anyway sufficient to reconstruct the visible domain of the plane wave spectrum, the singularity for

$k_z = 0$ , and a small circular region in the invisible domain. This spectral distribution provides very accurate results in the computed aperture field. The effect of an overmoding error has also been studied. It has been found that an overmode of the amplitude 0.1 and 0.2 can be detected and identified, in amplitude as well as in the phase, in the presence of typical measurement noise. Future investigations will concentrate on different antenna types with the purpose of identifying other antenna errors.

#### References

- [1] Kaplan L., Hanfling J. D., Borgiotti G. V., *The Backward Transform of the Near-Field for Reconstruction of Aperture Field*, IEEE Trans. on Ant. and Prop. Soc. Symp. Dig., pp 764-767, 1979.
- [2] Y. Rahmat-Samii, J. Lemanczyk, *Application of spherical near-field measurements to microwave holographic diagnosis of antennas*, IEEE Trans. on Ant. and Prop., vol 36, no 6, pp 869-878, June 1988.
- [3] Joy E. B., Guler M. G., *High Resolution Spherical Microwave Holography*, IEEE Trans. on Ant. and Prop., vol. 43, 464-472, 1995.
- [4] Cappellin C., Breinbjerg O., Frandsen A., *A high Resolution Antenna Diagnostics Technique for Spherical Near-Field Measurements*, 28<sup>th</sup> ESA Antenna Workshop, ESTEC, Noordwijk, The Netherlands, pp 899-906, 2005.
- [5] Cappellin C., Frandsen A., Breinbjerg O., *On the Relationship between the Spherical Wave Expansion and the Plane Wave Expansion for Antenna Diagnostics*, AMTA Europe Symposium, Munich, Germany, 2006.
- [6] Homepage of the DTU-ESA Facility: [http://www.oersted.dtu.dk/English/research/emi/afg/dtu\\_esa\\_facility.aspx](http://www.oersted.dtu.dk/English/research/emi/afg/dtu_esa_facility.aspx).
- [7] Hansen J. E., *Spherical Near-Field Antenna Measurements*, Peter Peregrinus Ltd. London, 1988.
- [8] Hansen T. B., Yaghjian A. D., *Plane Wave Theory of Time-Domain Fields, Near-Field Scanning Applications*, IEEE PRESS, 1999.
- [9] Devaney A. J., Wolf E., *Multipole Expansion and Plane Wave Representations of the Electromagnetic Field*, Journal of Math. and Physics, Vol. 15, 234-244, February 1974.
- [10] Homepage of TICRA's software: <http://www.ticra.com/script/site/page.asp?artid=27>.